Force-based many-body interatomic potential for ZrC

Ju Li
Department of Materials Science and Engineering, Ohio State University, Columbus, Ohio 43210

Dongyi Liao and Sidney Yip[a)]
Department of Nuclear Engineering, Massachusetts Institute of Technology, Cambridge, Massachusetts 02139

Reza Najafabadi and Lynne Ecker
Knolls Atomic Power Laboratory, Schenectady, New York 12309

(Received 31 October 2002; accepted 26 February 2003)

A classical potential for ZrC is developed in the form of a modified second-moment approximation with emphasis on the strong directional dependence of the C–Zr interactions. The model has a minimal set of parameters, 4 for the pure metal and 6 for the cross interactions, which are fitted to the database of cohesive energies of B1–, B2–, and B3–ZrC, the heat of formation, and most importantly, the atomic force constants of B1–ZrC from first-principles calculations. The potential is then extensively tested against various physical properties, none of which were considered in the fitting. Finite temperature properties such as thermal expansion and melting point are in excellent agreement with experiments. We believe our model should be a good template for metallic ceramics.
 [DOI: 10.1063/1.1567819]

I. INTRODUCTION

ZrC is a typical transition metal (refractory) carbide that takes B1 (NaCl) ground-state crystal structure at normal conditions with several notable characteristics[1]—exceptional hardness, very high melting point, chemically inert, and impervious to hydrogen attack. In addition, the material is extremely strong at high temperatures, highly nonstoichometric (large carbon vacancy concentrations), and exhibits metallic behavior in its electrical, magnetic, and optical properties. This family of ceramics is of considerable industrial interest, with significant structural, chemical, electronic, and nuclear applications.

Despite their technological interest, the extraordinary mechanical and thermal properties of ZrC have yet to be analyzed at the level of atomistic modeling and simulation. Such studies could play a significant role from the standpoint of developing a computational capability to predict the performance of the material under service conditions, typically earmarked by stress or thermal loading, or a radiation field. In contrast, SiC, another ceramic with a similarly wide range of applications, has been much more studied;[2–5] the difference here is the availability of an interatomic interaction description which is required for any large-scale atomistic calculation. Whereas tractable and reasonably realistic interaction potentials for SiC have been developed for some time,[6,7] no interatomic potential model for ZrC exists. Thus, the aim of the present work is to construct and validate an interatomic interaction description of ZrC for use in molecular dynamics simulations of mechanical and thermal behavior.

Since the robustness of any empirical potential is always a concern, our approach is to keep the model description as simple as the basic nature of Zr–C bonding would allow, while selecting a functional form of the interaction with a minimal set of parameters to be fitted. A crucial aspect is the focus on the Zr–C interaction force constants, treated as purely theoretically determined quantities, in the fitting procedure. As we will show by direct simulations using the constructed potential and comparing results with either experiment or theoretically more rigorous calculation, a range of different physical properties can be successfully predicted in this manner.

We begin in the next section with a discussion of chemical bonding characteristics in ZrC using Zr as a reference. In contrast to SiC in B3 (zinc blende)/B4 (wurtzite) polytype series where it is reasonable to apply the bond-order formulation developed for Si,[8] it is now important to recognize that ZrC and Zr are fundamentally quite different. From the chemical bonding considerations, it is clear that the strong angle-dependent interactions in ZrC should be treated as accurately as possible. In Sec. III the selection of a functional form of our potential which is capable of representing the known *N*-body character of interatomic interactions in refractory carbides is discussed; it is an extension to AB alloy of the second-moment form that has been applied to Zr.[9,10] Our model has six parameters specifying the Zr–C interaction. In Sec. IV we describe fitting the potential description to a database composed of cohesive energies of three structural phases of ZrC: B1, B2, and B3, elastic constants of B1–ZrC, force constant matrices for moving Zr or C in B1–ZrC, and the B1–ZrC heat of formation. In Sec. V the model thus constructed is used to calculate a set of properties—cohesive energy of ZrC in hexagonal B_h phase, point defect formation and migration energies, surface and vacancy relaxation, Grüneisen parameter and thermal expansion, vibrational amplitudes, and melting point—which are not in the fitting database and for which comparison with measurement or more rigorous calculation is made. Taken together, these

a)Electronic mail: syip@mit.edu

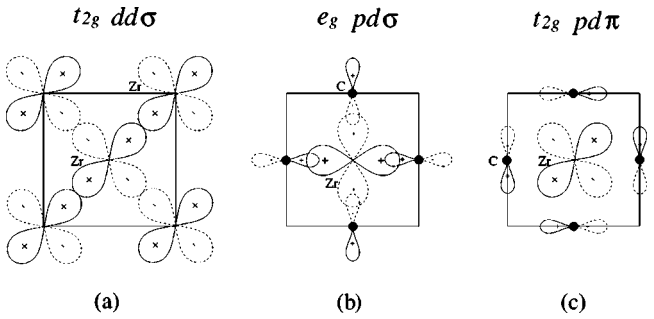

FIG. 1. Bond types in fcc pure Zr and B1–ZrC.

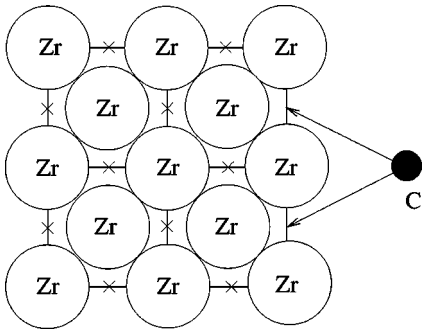

FIG. 2. An intuitive view of B1–ZrC_X.

results constitute a validation of the model. The article concludes with a brief discussion (Sec. VI) of applying the model to study strength and deformation behavior and thermal conductivity response of ZrC.

Currently there exists no empirical potential model of ZrC or any other refractory carbides, although a tight-binding description has been developed for TiC.[11,12] To accomplish this goal we have adopted an empirical approach based on first understanding the nature of ZrC bonding, then proposing an inspired functional form for the interaction, followed by fitting the parameters to a selected database of properties.

II. NATURE OF CHEMICAL BONDS

Group IV transition metals Ti,Zr,Hf have hexagonal close-packed ground-state structure at zero pressure. The electronic configuration of an isolated Zr atom is $5s^2 4d^2$. In condensed phases the *s* electrons can be promoted to *p* and *d* orbitals to occupy bonding states with the surrounding atoms. Exactly how that occurs depends on the local environment. In fcc pure Zr and B1–ZrC, the point group of the crystal field surrounding a Zr atom is O_h, under which the *d* orbitals split into two irreducible representations: t_{2g}: $\{xy,yz,zx\}$, and e_g:$\{x^2-y^2,3z^2-r^2\}$. In fcc Zr, the t_{2g} orbitals point toward the nearest-neighbor Zr atoms [bond type (a) in Fig. 1] and is lower in energy. To fully occupy them, each Zr atom needs three electrons, and so one *s* electron is promoted to the *d* band, leaving the other to the broader *sp* band. Essentially the same thing happens in hcp Zr which is a few hundredth of an electron volt/atom lower in energy than fcc Zr.[10] The electronic density of states of pure hcp Ti and Zr have been calculated by Lu *et al.*[13] Both are about 0.9 states/eV/atom at the Fermi level.

The pure fcc Zr is a relevant reference state for B1–Zr C_X (see Fig. 2) which is thermodynamically stable between $X=0.5$ and 1. Since Zr is more than twice as large as C by the Slater empirical radius (1.55 vs 0.7 Å),[14] one can think of ZrC_X as an fcc Zr lattice, with carbon atoms filling in the octahedral interstitial sites, without affecting much the total volume. Even if all the interstices are filled, C makes up only 11.6% of the total mass. Nonetheless, C has profound effects on the properties of the material, as can be seen from a comparison of elastic constants in Table I.

Pure Zr shows the behavior of a typical metal, large C_{12} and small C_{44} giving a positive Cauchy discrepancy ($C_{12}-C_{44}$)/B. With the addition of carbon, the bulk modulus is more than doubled. Even more significantly, C_{44} is nearly quintupled such that the Cauchy discrepancy is now negative, which is typical of ceramic materials. The fact that Zr C_X has an extremely high melting-point and is stable down to $X=0.5$, when C vacancies ''percolate'' and the fcc structure collapses, can be related to this extraordinarily large value of C_{44}. The elastic constants of TiC are also shown, and they are seen to be very close to those of ZrC.

Another indication of the strength of the hetero-nuclear bonding in ZrC is its large heat of formation: 2.14 eV/pair, in

$$\text{pure hcp Zr} + \text{graphite} \rightarrow \text{B1–ZrC}. \tag{1}$$

In comparison, the heat of formation in SiC is only 0.64 eV/pair. This and the change in elastic constants suggest that strong and highly angle-dependent bonds must exist between zirconium and carbon.

What are the nature of those bonds? Structurally, the B1 ground state may imply ionic bonding. While there had been controversy historically,[1] it is now clear that this is not the case. The properties of ZrC are dominated by the strong covalent bonds of $pd\sigma$ type shown in Fig. 1(b), assisted by weaker and slightly metallic $pd\pi$ bonds of the type shown in Fig. 1(c). Although there is appreciable charge transfer from Zr to C (0.42 electron),[12] it occurs in an isolated *sd* band 3.4 eV below the main band[17] with metallic screening neutralizing its effect. Ionic bonding and the original metal–metal $dd\sigma$ bonds are sufficiently weak in ZrC that they can be neglected in the first approximation. The essence of bonding in ZrC therefore lies in how the (b) and (c) bond types in Fig. 1 replace the (a) bond type of pure Zr to receive the boon of chemical affinity manifested in the heat of formation, and what demands of the local atomic environment in order to receive it.

Jhi *et al.* calculated the total and symmetry-decomposed electron density of states in TiC using full potential linear muffin-tin orbital (LMTO) method.[17] At the Fermi level, the total density of states (DOS) is 0.24 states/eV/atom, which is about 1/4 of that in hcp Ti. Below the Fermi level, C *p*- and Ti *d*-local DOS (LDOS) show a strong correlation, indicating the formation of substantial chemical bonding in which the Ti $d-$LDOS can be further decomposed into e_g and t_{2g} parts. We see that the e_g *d*-LDOS is in general larger than the t_{2g} *d*-LDOS, but it drops to zero at the Fermi level and is clearly split between the occupied bonding and the unoccu-

TABLE I. Elastic constants of hcp and fcc Zr, ZrC, and TiC. The first four columns are from experiment and *ab initio* calculations. The fifth column is from a tight-binding potential for TiC (see Ref. 12). The last column is from our empirical potential for ZrC.

GPa	hcp Zr[a]	fcc Zr[b]	B1–ZrC[c]	B1–TiC[d]	B1–TiC (TB)[d]	B1–ZrC (present)
C_{11}	155.4	119	480.2	515	313	381.1
C_{12}	67.2	77	101.8	106	207	121.0
C_{44}	36.3	53	169.7	179	119	177.7

[a]See Ref. 10.
[b]See Ref. 15.
[c]See Ref. 16.
[d]See Ref. 12.

pied antibonding states, which means that the $pd\sigma$ bond between C and Ti is purely covalent. On the other hand, the Ti t_{2g} *d*-LDOS, though weaker, is nonzero at the Fermi level, and it correlates with the nonzero C *p*-LDOS at the Fermi level. Thus, $pd\pi$ bonding between C and Ti is slightly metallic, which accounts for the fact that TiC is electrically conductive. The original Ti–Ti $dd\sigma$ bond plays little role in this electrical conductivity; it is very small below the Fermi level. Only when C is removed from the system does the $dd\sigma$ bond begin to have a more significant influence. Thus we cannot totally ignore it if we want to study the dependence on stoichiometry.

If the main band is integrated, one finds[12] that 3.01 electrons occupy the C *p* and 2.99 electrons occupy the Ti *d* orbitals, thereby confirming the rule of local charge neutrality in metallic alloys.[26] However, there is an isolated and narrow band 3.4 eV below the main band that has 1.41 electrons occupying the C *s* orbitals and 0.59 electrons occupying the Ti *d* orbitals, which accounts for the total of eight valence electrons of a Ti/C pair. Importantly, no sign of sp hybridization on C of the types that occur in diamond or graphite is ever observed.

The crucial question is, why do $pd\sigma$ bonds and to a lesser degree $pd\pi$ bonds, favor the octahedral arrangement and strongly resist shear? This clearly has do with C, because pure Zr has a very small C_{44}. Let us consider the reference case of diamond where sp^3 hybridization favors the tetrahedral arrangement. It penalizes shear deformation relatively severely as compared to metals, because unlike volumetric deformation, shear strain destroys the orthogonality of hybridized orbitals in Hilbert space. Now recall that sp^3-bonding orbitals achieve orthogonality in Hilbert space without requiring them to be orthogonal in real space (bond angle 109.47°) due to participation of the *s* orbital

$$|h_{[111]}\rangle = |s\rangle + |p_x\rangle + |p_y\rangle + |p_z\rangle,$$
$$|h_{[1\bar{1}\bar{1}]}\rangle = |s\rangle + |p_x\rangle - |p_y\rangle - |p_z\rangle,$$
$$|h_{[\bar{1}1\bar{1}]}\rangle = |s\rangle - |p_x\rangle + |p_y\rangle - |p_z\rangle,$$
$$|h_{[\bar{1}\bar{1}1]}\rangle = |s\rangle - |p_x\rangle - |p_y\rangle + |p_z\rangle.$$

Without hybridizing with the *s* orbital as the LDOS clearly shows, the local orbitals on carbon pointing to the Zr neighbors composed of *p* states only, necessarily have to be mutually orthogonal in real space in order to remain orthogonal in Hilbert space. Whenever that cannot be satisfied, the two $pd\sigma$ bonds involved should both be significantly reduced in strength. Therefore, the octahedral arrangement with six Zr nearest neighbors is the maximum that a C atom can accommodate with the orthogonality criterion. If more neighbors are added, it would not receive nearly as much benefit in band energy as it does previously due to the unavailability of *p* orbitals, whereas core repulsion would make this overcoordination attempt energetically unfavorable.

Thus, a critical aspect of a successful potential for ZrC_X is the same as those for Si or C, whether it is formulated empirically[6,18,19] or through an approximate formalism,[20–23] which is how does one correctly describe the angular dependence of bonding, or bond interference effect. We note that based on density functional theory (DFT), the actual total energy is outcome of minimizing a nonlinear, complex functional, and the ''apparent'' electron Hamiltonian is strongly dependent on the self-consistent charge density. A simple tight-binding approach with radially dependent but angular-independent matrix elements is often incapable of describing a large set of atomic environments, so explicitly angular-dependent matrix elements have been introduced to the tight-binding approach as well.[24]

III. THE POTENTIAL MODEL

The Finnis–Sinclair potential[25] based on the second-moment approximation[26] has been applied to modeling transition metals and their alloys during the past two decades. Willaime and Massobrio[9] (WM) have fitted a second-moment potential for Zr with only four adjustable parameters. It has been shown to give reasonable results for defect formation and migration, thermal expansion and phonon properties in both hcp and bcc Zr. In particular, it is able to capture the temperature-dependent phonon anomalies in bcc Zr that are related to the hcp → bcc transition.[10] Later the model was used to study fast diffusion of impurities in hcp Zr with additional parameterization for Ni–Ni and Ni–Zr interactions.[27]

We have adopted the WM potential as the basis to develop an empirical potential for Zr/C. Keeping to its tradition of simplicity, we will work toward finding a minimal set of additional parameters. As we have discussed, angular dependence lacking in the WM potential must now be introduced to reflect the fundamental change in nature of bonding from pure Zr to ZrC_X. After trials with sets of 7–11 parameters, we find that six parameters are sufficient to describe the Zr–C bonding, 2 each for core repulsion and hopping strength, and just 2 for the angular dependence. There is no

explicit C–C term[28] because the carbon separations in ZrC are well beyond their normal bond distance cutoffs, and attempting to fit them would lead to artifacts. Based on the discussion in Sec. II, a more plausible physical mechanism can be proposed to explain the C–C force constants in ZrC without resorting to direct C–C bonding. This approach fits well the results of a DFT calculation.[16] As the number of free parameters in the fitting decrease from 11 to 6, there is a gradual but appreciable increase in the fitting error. Nevertheless we maintain our emphasis on the minimal set of parameters and considered only those that are the most indispensable.

A. Second-moment approximation for pure Zr

The moments theorem derived by Cyrot–Lackmann[29] based on the tight binding (TB) formalism expresses the idea that the spread (and higher-order shape factors) of the valence electron LDOS at an atomic orbital is directly related to its ''interactions,'' or matrix elements, with neighboring orbitals, thus providing a theoretical basis for the local interaction approach that is used by all empirical potentials. Assuming one generic atomic orbital at each site, labeled by i or j, one can write for the interaction between two sites,

$$h_{ij} \equiv \langle i|\mathcal{H}|j\rangle, \quad e_i \equiv h_{ii}, \tag{2}$$

where $\mathcal{H}$ is the self-consistent valence electron Hamiltonian, and $|i\rangle$ is a Wannier orthogonal function.

The system's total energy E^{tot} can be expressed as[30]

$$E^{\mathrm{tot}} = E^{\mathrm{rep}} + E^{b}, \tag{3}$$

in the tight binding formulation, where E^{rep} is the repulsive energy due to overlapping cores, and the attractive band structure energy

$$E^{b} \equiv \int^{E_F} dE \rho(E) E \tag{4}$$

describes the valence electron bonding which provides cohesion. In the second-moment approximation the band structure energy has the form

$$E^{b} = \sum_i E_i^b = -\sum_i f_{\alpha_i} \sqrt{\sum_{j\neq i} |h_{ij}|^2}. \tag{5}$$

The second-moment approximation provides some insights into the many-body potentials for metals, especially for transition metals with narrow d band. For an elemental metal, the constant f_{α_i} can be absorbed into h_{ij} and need not to be fitted separately. For an alloy, f_{α_i} can also be absorbed, but we would then lose the symmetry $h_{ij} = h_{ji}$.

It is common practice in tight-binding theory to assume that the core repulsion E^{rep} in Eq. (3) is the sum of pair interactions

$$E^{\mathrm{rep}} = \sum_i \left[\sum_{j\neq i} \phi_{\alpha_i\beta_j}(r_{ij}) \right], \tag{6}$$

for which a simple exponential form $a_{\alpha\beta}\exp(-b_{\alpha\beta}r)$ is often sufficient.

The conceptual proposition of the Finnis–Sinclair potential is that h_{ij} in Eq. (5) can be represented by a radial function $h_{\alpha_i\beta_j}(r_{ij})$. To certain extent this is a reasonable approximation for Zr, for the following reason. There are five d orbitals at every atom, and each d orbital has four lobes (except $3z^2-r^2$) that can point to four neighbors simultaneously, so overall there is less shortage of empty orbitals that can bond with a new neighbor, and which still remains largely orthogonal to the other occupied bond orbitals in Hilbert space. In contrast, in ZrC, the availability of C p orbitals is a critical issue because there are only three p orbitals at each site and a p orbital has only two lobes that can form a σ bond with neighbors. Therefore, it is not surprising that while $h_{ij} = h(r_{ij})$ may be a good approximation for Zr–Zr, it is less so for the Zr–C bonds.

For metals, a properly parametrized second-moment potential can impart significant improvements over pair potentials. Foremost, the many-body effect of saturation is built in. If an atom has Z neighbors, the bonding energy is $\propto\sqrt{Z}$ instead of $\propto Z$ as a pair potential would give. This means that lower coordination number structures like the bcc phase may be stabilized against the fcc phase. The strength of an individual bond, that is, how much force a bond could convey when a neighbor is displaced, is now $\propto 1/\sqrt{Z}$, which is the same for the energy benefit of adding a new neighbor. Second, the fact that Eq. (5) is derived from quantum theory is reflected naturally in its elastic properties. A pair potential can only give $C_{12} = C_{44}$. Without much effort, most second-moment potential parameterizations can give a C_{12} that is significantly greater than C_{44}, found in most metals. Last, in terms of computational cost, it is on the same order as a pair potential, in fact no more than twice as expensive.

TABLE II. Parameters of WM potential in the form of Eq. (8).

a (eV)	r_c (Å)	p	r_0 (Å)	ξ (eV)	q
0.179 364	6.8	9.3	3.1744	2.201 454 8	2.1

WM published their potential for Zr in 1989:[9]

$$E^{\mathrm{tot}} = \sum_i V_i, \tag{7}$$

$$V_{\mathrm{i}} = \left\{ a \sum_{r_{ij}<r_c} \exp\left[-p\left(\frac{r_{ij}}{r_0} - 1 \right) \right] \right\} - \left\{ \sum_{r_{ij}<r_c} \xi^2 \exp\left[-2q\left(\frac{r_{ij}}{r_0} - 1 \right) \right] \right\}^{1/2}, \tag{8}$$

with the parameters listed in Table II. r_0 is the nearest-neighbor distance of hcp Zr at $T=0$ so it is not a free parameter. A sharp distance cutoff of $r_c = 6.8$ Å is picked so as to ensure the correct hcp vs bcc, fcc stability.

Within the electron volt–angstrom unit system, Eq. (8) can be reexpressed in a simpler form

$$V_{\mathrm{i}} = \left\{ \sum_{r_{ij}<r_c} \exp[A(B - r_{ij})] \right\} - \left\{ \sum_{r_{ij}<r_c} \exp[C(D - r_{ij})] \right\}^{1/2} (\mathrm{eV}), \tag{9}$$

TABLE III. Parameters of the reorganized WM potential Eq. (9) in the eV–Å unit system.

A_{ZrZr} (Å^{-1})	B_{ZrZr} (Å)	C_{ZrZr} (Å-1)	D_{ZrZr} (Å)
2.929 687 5	2.587 873 956 389 39	1.323 084 677 419 35	4.367 246 426 256 3

where

$$A \equiv \frac{p}{r_0}, \quad B \equiv r_0\left[1+\frac{\log(a)}{p}\right], \quad C \equiv \frac{2q}{r_0},$$
$$D \equiv r_0\left[1+\frac{\log(\xi)}{q}\right]. \tag{10}$$

Thus, there are only four free parameters in the model if one excludes r_c. These are listed in Table III.

B. Empirical potential for Zr/C

To empirically extend the second-moment potential to AB alloys, it is common to write,[27,31–33] by neglecting the on-site energy differences

$$E^{\text{tot}} = \sum_{i\in A} V_i + \sum_{i\in B} V_i,$$

$\forall i \in$ A:

$$V_i = \sum_{j\in A\neq i} \phi_{AA}(r_{ij}) + \sum_{j\in B} \phi_{AB}(r_{ij}) - X_i^{1/2},$$

$$X_i = \sum_{j\in A\neq i} h_{AA}^2(r_{ij}) + \sum_{j\in B} h_{AB}^2(r_{ij}),$$

$\forall i \in$ B:

$$V_i = \sum_{j\in A} \phi_{BA}(r_{ij}) + \sum_{j\in B\neq i} \phi_{BB}(r_{ij}) - X_i^{1/2}, \tag{11}$$

$$X_i = \sum_{j\in A} h_{BA}^2(r_{ij}) + \sum_{j\in B\neq i} h_{BB}^2(r_{ij}),$$

where

$$\phi_{AB}(r_{ij}) = \phi_{BA}(r_{ij}), \tag{12}$$

and one may stipulate

$$h_{AB}^2(r_{ij}) = h_{BA}^2(r_{ij}). \tag{13}$$

Our Zr/C potential follows the form of Eq. (11) with A=Zr and B=C, with several important modifications.

(1) Unlike $h_{ZrZr}(r)$, the so-called bare strength $h_{ZrC}(r)$ would not be directly used in Eq. (11). Instead, the so-called screened strength $\tilde{h}_{ZrC}$ would take its place, whose value is h_{ZrC} scaled by an interference factor depending on h_{ZrC} strengths nearby and respective angular cosines. The concept of angular dependence and screening has long been introduced to empirical potentials for metals and alloys.[20–22]

(2) The bare strength is supposed to be the overlap matrix element when both atoms have bonding orbitals available pointing at each other. For Zr–Zr this is not a big problem, but for Zr–C it is severely constrained by the limited availability of carbon *p* orbitals, and its orthogonality preference in Hilbert space and therefore in real space.

(3) h_{ZrC} must be stronger than h_{ZrZr}, but it also must be short ranged. A cutoff distance of $r_c^{ZrC}=3.5$ Å is imposed arbitrarily, which is midway between the first and third nearest neighbors in B1–ZrC (both of Zr–C type interactions).

(4) We set $h_{CC}=\phi_{CC}=0$, which differs from the cohesive energy model of Cottrell.[28] There is no evidence of direct C–C bonding in ZrC. C–C distances in ZrC ($\sim$3.3 Å) are considerably larger than their normal cutoff distances ($\sim$2.1 Å),[6,19,34] and the size of the Zr atom should provide excellent screening. The energy benefit of Zr–C bonding is so great that the carbon electrons should predominantly concentrate on Zr–C bonds in a Zr-rich environment. If one needs to study a C-rich environment such as the interface between certain form of pure carbon with ZrC_X, then one is free to pick any pure C potential[6,19,34] to describe the C–C direct bond. Due to its rare occurrence in ZrC_X, we do not take upon ourselves the responsibility of fitting the C–C direct bond, although we have made sure that the ZrC heat of formation is correct when the experimental value of graphite's cohesive energy is used. In other words, in order to have the correct global thermodynamic driving force in a pure C/pure Zr interface simulation, one just needs to make sure that his pure C potential reproduces the experimental cohesive energy of graphite.

(5) We use a simple exponential form for both $\phi_{\alpha\beta}(r)$ and $h_{\alpha\beta}(r)$ following the WM potential. Since this potential has no provision for a smooth cutoff, we impose a scheme on all radial functions by multiplying them with $e^{K/(r-r_c)}$ with an arbitrarily picked $K=0.1$ Å, making all radial derivatives continuous at $r=r_c$. The original $r_c^{ZrZr}=6.8$ Å is shifted to $r_c^{ZrZr}=7$ Å to accommodate this change. We have found no significant differences in the pure Zr properties, including hcp/bcc/fcc phase stabilities, after this modification.

(6) We take the constraint $h_{ZrC}(r)=h_{CZr}(r)$ to save one parameter, as we have insufficient data to support it.

In summary, $\phi_{CC}(r)=h_{CC}(r)=0$, and

$$\phi_{ZrZr}(r) = \exp\left[A_{ZrZr}(B_{ZrZr}-r)+\frac{K}{r-r_c^{ZrZr}}\right](\text{eV}),$$
$$h_{ZrZr}^2(r) = \exp\left[C_{ZrZr}(D_{ZrZr}-r)+\frac{K}{r-r_c^{ZrZr}}\right](\text{eV}^2), \tag{14}$$

where $K=0.1$ Å, $r_c^{ZrZr}=7$ Å, and A_{ZrZr}, B_{ZrZr}, C_{ZrZr}, and D_{ZrZr} are listed in Table III. Furthermore

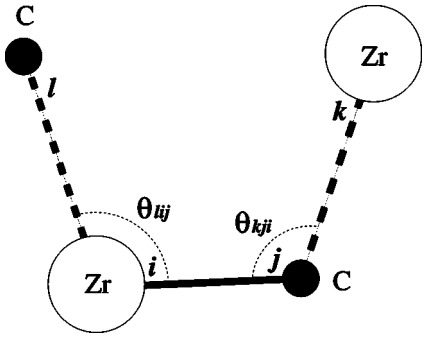

FIG. 3. An illustration of the Zr–C bond screening.

$$\phi_{\mathrm{ZrC}}(r)=\phi_{\mathrm{CZr}}(r)=\exp\left[A_{\mathrm{ZrC}}(B_{\mathrm{ZrC}}-r)+\frac{K}{r-r_c^{\mathrm{ZrC}}}\right](\mathrm{eV}),$$
$$h_{\mathrm{ZrC}}(r)=h_{\mathrm{CZr}}(r)=\exp\left[C_{\mathrm{ZrC}}(D_{\mathrm{ZrC}}-r)+\frac{K}{r-r_c^{\mathrm{ZrC}}}\right](\mathrm{eV}), \quad (15)$$

with $r_c^{\mathrm{ZrC}}=3.5$ Å, and A_{ZrC}, B_{ZrC}, $\mathrm{C}_{\mathrm{ZrC}}$, and D_{ZrC} are to be fitted.

After a number of trials, we decide that the screening of h_{ZrC} should take the form

$$\tilde{h}_{\mathrm{ZrC}}(i=\mathrm{Zr},j=\mathrm{C})=h_{\mathrm{ZrC}}(r_{ij})\times\exp\left[-\frac{\sqrt{s_{ij}}}{h_{\mathrm{ZrC}}(r_{ij})}\right], \quad (16)$$

where i is the Zr atom and j is the C atom of a Zr–C bond, and the screening strength s_{ij} is

$$s_{ij}\equiv\sum_{l\in\mathrm{C},l\neq j}\left(\frac{1+\cos\theta_{lij}}{\alpha_{\mathrm{ZrC}}}\right)^{\beta_{\mathrm{ZrC}}}h_{\mathrm{ZrC}}^2(r_{il})+\sum_{k\in\mathrm{Zr},k\neq i}\left(\frac{1+\cos\theta_{kji}}{\alpha_{\mathrm{CZr}}}\right)^{\beta_{\mathrm{CZr}}}h_{\mathrm{ZrC}}^2(r_{jk}), \quad (17)$$

where the l's are all the C atoms that interact with i, besides j, and the k's are all the Zr atoms that interact with j besides i (see Fig. 3). For the sake of minimal set we have further taken $\alpha_{\mathrm{ZrC}}=\alpha_{\mathrm{CZr}}$ and $\beta_{\mathrm{ZrC}}=\beta_{\mathrm{CZr}}$, so we are left with only two screening parameters to fit. Equation (16) participates equally in the X sums of both the C and Zr atoms, as shown in Eqs. (11) and (13).

The meaning of Eqs. (16) and (17) can be seen from the following considerations.

(1) How strongly the ij matrix element is screened depends on the bare strengths of the screening bonds: il or jk. We cannot have a new neighbor just entering the cutoff to strongly screen the other bonds that are much closer to i or j. Therefore s_{ij} must depend on $h_{\mathrm{ZrC}}(r_{il})$ and $h_{\mathrm{ZrC}}(r_{jk})$ in some fashion. As normalization, $h_{\mathrm{ZrC}}(r_{ij})$ ends up in the denominator.
(2) $\sqrt{s_{ij}}$ is used instead of s_{ij} in Eq. (16) because physically $h_{ij}=\langle i|\mathcal{H}|j\rangle$, a complex quantity that cannot be summed. But h_{ij}^2 can be interpreted as $|\langle i|\mathcal{H}|j\rangle|^2$, which can be summed.
(3) For the angular dependence, we use the simplest form available. β_{ZrC} will be large, and the screening is practically nonexistent when $\theta\geqslant 2\pi/3$, but it rises dramatically when $\theta<\pi/2$.

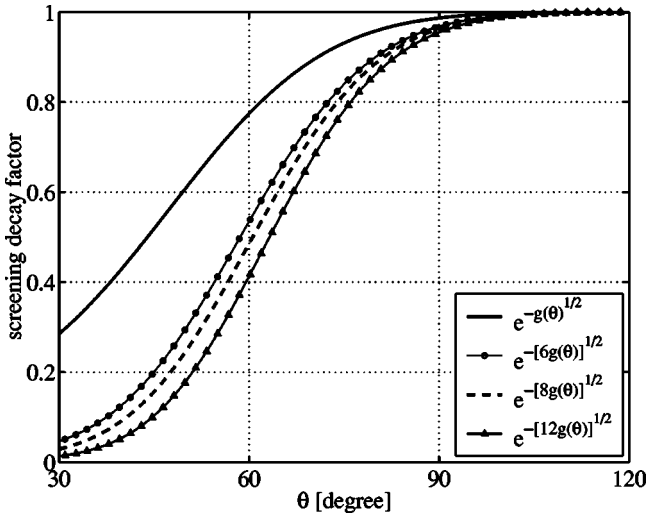

FIG. 4. Illustration of the screening decay factor $\exp(-\sqrt{s_{ij}})$ (assuming all h's are equal).

We will discuss the procedure and results of fitting Eqs. (15) and (17) in the next section. Here we give the optimized parameters in Table IV. The physically significant digits are of course much less than shown, but we keep the digits for numerical calibration purposes.

Using the optimized parameters, the screening decay factor $e^{-\sqrt{s_{ij}}}$ is illustrated in Fig. 4, taking all h's to be of equal strength. In B1–ZrC, for each Zr–C bond there are $2\times4=8$ other Zr–C bonds attached, with bond angle $\sim\pi/2$ (two other bonds with angle $\sim\pi$ have little effect), so $e^{-\sqrt{8((1+\cos\theta)/\alpha_{\mathrm{ZrC}})^{\beta_{\mathrm{ZrC}}}}}$ is plotted as an illustration of the magnitude and stiffness of the screening, and similarly, for $2\times3=6$ (B3 structure) at $\theta\sim109.47°$ and $2\times6=12$ (B2 structure).

Figure 5 shows the bare strengths $2\phi_{\mathrm{ZrZr}}(r)$, $-h_{\mathrm{ZrZr}}(r)$, $2\phi_{\mathrm{ZrC}}(r)$, $-h_{\mathrm{ZrC}}(r)$. Note that ϕ and h are not directly comparable, because the effect of ϕ increases linearly with coordination Z, while that of h increases as $\propto\sqrt{Z}$.

TABLE IV. Optimized parameters of Eqs. (15) and (17) in the eV–Å unit system.

A_{ZrC} (Å^{-1})	B_{ZrC} (Å)	$\mathrm{C}_{\mathrm{ZrC}}$ Å^{-1})	D_{ZrC} (Å)
3.245 893 936 698 54	2.056 798 049 191 17	0.823 038 180 523 68	4.154 822 258 151 34
α_{ZrC}	β_{ZrC}		
1.808 533 038 462 49	14.593 454 943 734 51		

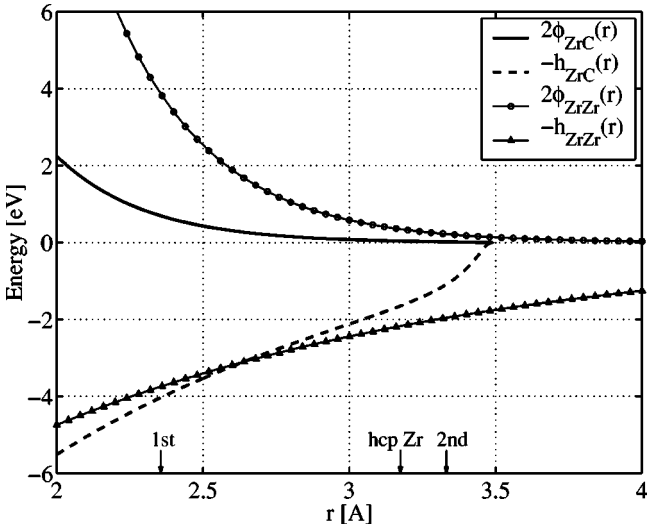

FIG. 5. Radial functions of bare strengths. The 1st arrow is at the nearest neighbor distance (Zr–C) in zero-pressure B1–ZrC; the 2nd arrow is at the second-nearest neighbor distance (Zr–Zr) in zero-pressure B1–ZrC. The "hcp Zr" arrow is at the nearest neighbor distance (Zr–Zr) in zero-pressure hcp Zr.

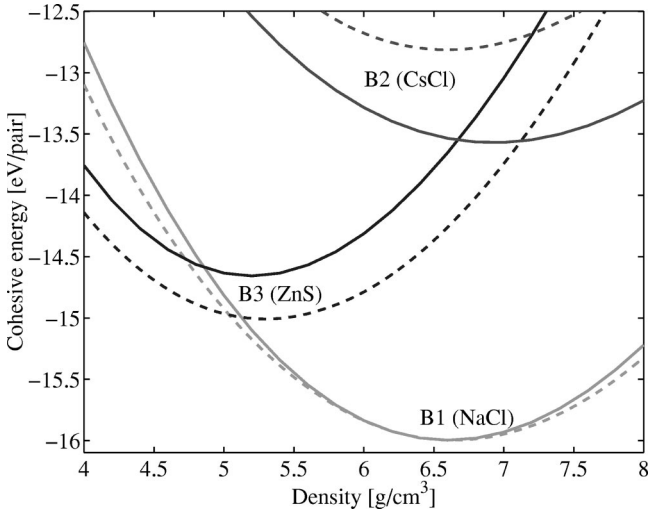

FIG. 6. Cohesive energy curves of three cubic phases of ZrC. Solid lines are from DFT calculations (shifted vertically to match $E^{\mathrm{B1-ZrC}}_{\mathrm{equilibrium}}$), dash lines are from the present empirical potential.

They are plotted together in Fig. 5 only for illustration purposes.

Finally, we caution that when a bond breaks (r_{ij} exceeds r_c^{ZrC}) and $h_{\mathrm{ZrC}}(r_{ij})$ drops to zero, there is no problem mathematically having $h_{\mathrm{ZrC}}(r_{ij})$ at the denominator inside Eq. (16). Numerically, though, it is wise to test whether $\sqrt{s_{ij}}/h_{\mathrm{ZrC}}(r_{ij}) < 50$ before feeding it to the exponential; if not then the function value and all derivatives can be taken to be zero. The same is also true for the smooth cutoff function $e^{K/(r-r_c)}$.

IV. THE FITTING PROCEDURE

The six Zr–C interaction parameters tabulated in Table IV have been fitted to:

(a) the cohesive energy curves of B1–, B2– and B3-ZrC;
(b) the elastic constants of B1–ZrC;
(c) the force constant matrices of moving either a Zr or a C atom in B1–ZrC; and
(d) the B1–ZrC heat of formation,

in which fitting to (c) is the most instructive.[35] We find that if we only fit to (a),(b),(d), then even a binary pair potential can do a reasonable job except $C_{12}=C_{44}$. However, when we compare the pair potential's force constants with the DFT results,[16] we discover they are grotesquely wrong. The spatial distribution of the DFT force constants reveals so much about the nature of Zr–C bonding in ZrC that without it we would never arrive at our present model Eqs. (16) and (17).

(a)–(d) are fitted jointly by defining an error function which is the weighted average of the relative errors between the values given by our potential with a certain parameter set and the target values for the same properties. This complementary error function is then minimized in the parameter space by using either selective directed search or simulated annealing. In practice, the model development and the numerical optimization were done iteratively, and it was never an easy process. One must constantly open the black box of the fitting code and plot out the relevant variables for typical atomic environments, in order to gradually form an intuitive picture of how the model operates. Only after many trials and errors do we settle on Eqs. (16) and (17) and Table IV. The fitted properties are discussed next in detail.

The cohesive energies of B1–, B2–, and B3–ZrC, corresponding to coordination numbers 6, 8, and 4, are plotted in Fig. 6 as a function of density. The reference curves are calculated using VASP[36] with the Perdew–Wang generalized gradient (GGA) exchange-correlation density functional[37] and ultrasoft pseudopotential.[36] Both the energy-cutoff and **k**-point convergence have been carefully verified. B2 and B3 structures are chosen because they represent over- and undercoordinated environments that may appear locally in B1–ZrC's defects. The goal is to interpolate over sufficient number of reference environments so the interatomic potential can behave well in not-fitted but characteristically similar environments. Ideally, a careful fit to reference environments with coordination numbers ranging from 2 to 12 can produce very robust environment-dependent potentials.[24]

The elastic constants of B1–ZrC at $P=0$ are given in the rightmost column of Table I. They are significantly improved over the tight-binding results for B1–TiC[12] whose hopping integrals do not have angular dependence. Specifically, our $C_{44} \gg C_{12}$, whereas their $C_{12} \gg C_{44}$, under the constraint that both give the same bulk modulus.

A DFT calculation by Jochym and Parlinski[16] has provided atomic force constant information for B1–ZrC which we will use as fitting targets. We obtain force constants by setting up a large cell, moving the atom (C or Zr) at the origin by a small amount, and calculating the forces on the surrounding atoms. Due to cubic symmetry, one small displacement in the x direction is sufficient.

Results of the fitted force constants are shown in Figs. 7 and 8 for C and Zr, respectively, along with DFT target values. The agreement is generally quite satisfactory. Notice that in the DFT results the four neighbors in the transverse

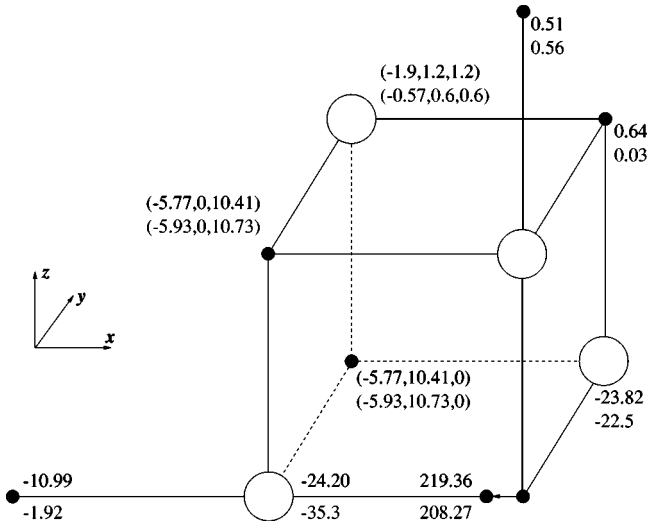

FIG. 7. C atom force constants in B1–ZrC in unit of N/m. Jochym *et al.*'s DFT results (see Ref. 16) are the numbers above, present results are the numbers below. Only the atoms that contribute significantly to the total reaction force are shown, and some are omitted by symmetry.

plane of the displacement offer as much resistance per atom as the two neighbors directly in line with the displacement. This, supports the idea of very strong bond angle dependence. If one were to use an optimized pair potential, as we have, one would find that this essential feature cannot be realized, as the atom directly ahead of the displacement always offers >3 times more resistance than the transverse plane atoms. In other words, although a binary Lennard–Jones or a Morse potential is able to give satisfactory cohesive energy curves and C_{11}, $C_{12}=C_{44}$, they are bound to fail to account properly for the local interactions. Cauchy discrepancy originates from two sources, many-body interactions and bond angle forces: the former tends to give positive contribution while the latter tends to give negative contribution.[38] The atomic force constants provide spatial and vectorial details which are otherwise covered up in the scalar total energetics. They are highly sensitive characteristics of the nature of the chemical bonds.

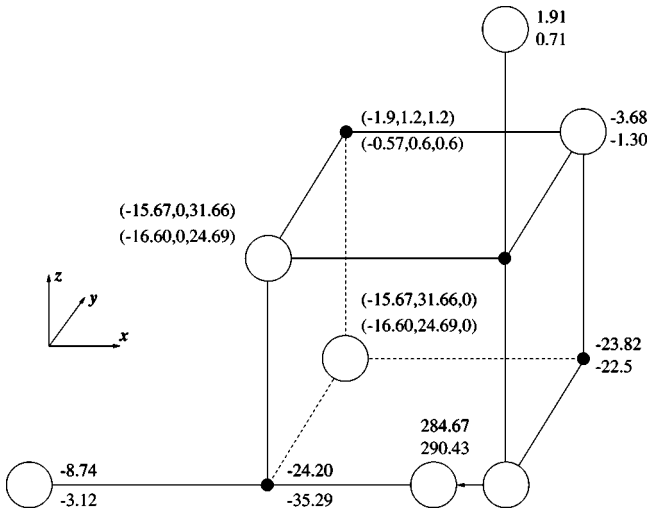

FIG. 8. Same as Fig. 7 except Zr atom is displaced.

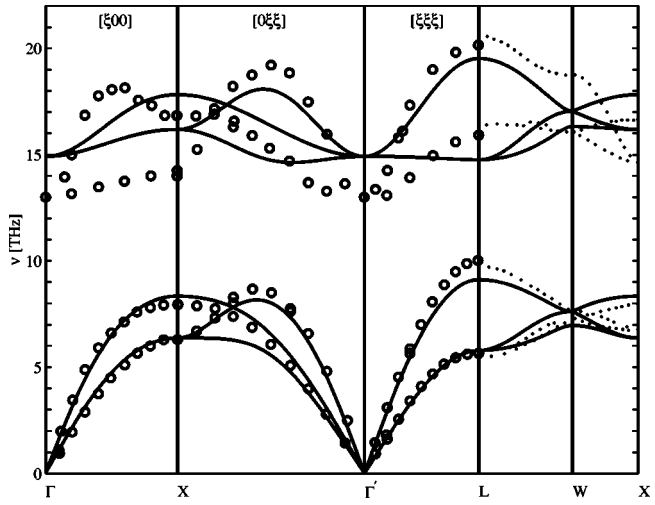

FIG. 9. Phonon dispersion curve of ZrC, comparing present results (solid line) with experiment (see Ref. 40) (circles), and DFT calculations (see Ref. 16) (dots).

The phonon dispersion curve[39] of ZrC is plotted in Fig. 9, along with experimental results[40] and results from Jochym *et al.*'s DFT calculations.[16] The agreement is quite good for the acoustic branches, and satisfactory for the optical branches. The overall quality of agreement is better than that of the Tersoff potential for SiC.[4]

Phonon DOS and LDOS are shown in Fig. 10. They are in good agreement with the results of Jochym *et al.*[16] Especially, the Zr atom LDOS almost completely fills the acoustic band while the C atom LDOS almost completely fills the optical band. This almost-decoupled LDOS feature is somewhat counterintuitive since the Zr and C atoms interact strongly. We attribute this to the large mass difference between Zr and C. The C atom is effectively isolated in a Zr cage, rattling with high frequencies like an independent oscillator, whereas the Zr atoms ''see'' other Zr atoms and vibrate coherently as acoustic phonons.

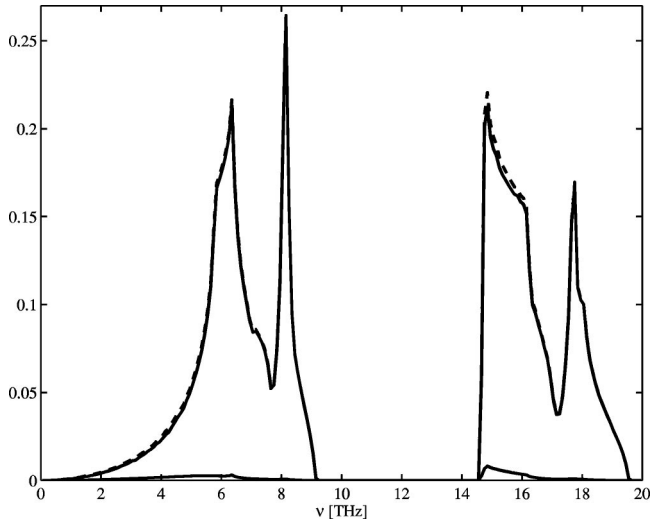

FIG. 10. Phonon DOS (dash line) and LDOS (full lines) in ZrC. Zr atom LDOS almost completely fills the acoustic band, while the C atom LDOS almost completely fills the optical band.

TABLE V. Comparison of the equilibrium structure and lattice stability for the hexagonal B_h phase.

	c/a	$E_{B_h}-E_{B1}$ (eV/atom)
FPLMTO (B_h–TiC)[a]	0.86	0.78
TB (B_h–TiC)[b]	0.67	0.21
Present (B_h–ZrC)	0.97	0.56

[a]See Ref. 44.
[b]See Ref. 12.

TABLE VI. Carbon vacancy formation and migration energies in B1–ZrC/TiC.

	Formation (eV)	Migration (eV)
TB (TiC)[a]	1.50	2.66
VASP (ZrC)	1.16	···
Present (ZrC)	1.51	4.86

[a]See Ref. 47.

Using the GGA density functional and ultrasoft pseudopotential,[36] we compute the total energies of hcp Zr, graphite and B1–ZrC, and obtain a heat of formation value of 1.72 eV/pair for Eq. (1). In comparison, Guillermet's experimental result is 2.14 eV/pair.[41] The present model fits to the experimental value and the result is 2.47 eV/pair (graphite's cohesive energy is taken to be 7.43 eV/atom). The heat of formation reflects the strength of the chemical bond and is closely related to the thermal and chemical stability of the compound. The large value in ZrC makes it very stable, having one of the highest melting points known.

V. THE VALIDATION PROCEDURE

To validate the potential model, we investigate several properties that have not been used in the fitting procedure in any way. Due to the scarcity of experimental data available on ZrC, we find it useful to also include some TiC data. Ti and Zr are transition metals belonging to the $3d$ and $4d$ series, respectively, both being group IVA elements. Thus, they have similar electronic structure which in turn leads to similar physical properties such as elastic properties (see, for example, a critical review by Kral *et al.*[42] and also Table I, as well as thermal conductivity).[43] This similarity of physical properties extends to families of metallic ceramics and includes nitrides, and borides, as well as carbides.

A. Hexagonal B_h phase

The B_h–ZrC structure provides a good test of the transferability of our potential, because only three cubic phases were considered in the fitting (Fig. 6). The B_h structure is also called WC structure because it is the ground state of the tungsten–carbon compound which supplants the B1 structure as the ground state when going from group IV to VI transition metal carbides.[44] The c/a and $E_{B_h}-E_{B1}$ predictions from the present model are tabulated in Table V, along with the full-potential LMTO (FPLMTO)[44] and tight-binding[12] results for B_h–TiC. The tight-binding $E_{B_h}-E_{B1}$value appears to be too low.

B. Carbon vacancy formation and migration energies

Using the GGA density functional and ultrasoft pseudopotential,[36] we compute the carbon vacancy formation energy, defined here as the energy cost of removing one carbon atom from B1–ZrC bulk and place it in graphite. We use a 63-atom supercell and $7\times7\times7$ Monkhorst–Pack[45] **k** sampling. The planewave basis has an energy cutoff of 358.4 eV. Ion relaxation terminates when the energy change between two steps is less than 1 meV, and the maximum force on one atom is less than 0.01 eV/Å. We get $E_f(V_C)=1.16$ eV from VASP. In comparison, the present model gives $E_f(V_C)=1.51$ eV.

Following Baskes *et al.*,[46] we have also computed the forces on atoms near an unrelaxed carbon vacancy. To our surprise, even though the agreement in E_f is reasonable between VASP and the present model, there is a large discrepancy in the unrelaxed forces. In both cases only the six Zr atoms near the unrelaxed carbon vacancy sustain appreciable force. However, VASP gives 1.65 eV/Å outward expansion force per atom, while the present model gives only 0.61 eV/Å. Energy decrease during the relaxation: $E_f^{\text{unrelax}}(V_C)-E_f(V_C)$, is 0.43 eV in VASP and only 0.079 eV in the present model.

For the carbon vacancy migration energy, we follow the approach used by Harris and Bristowe[47] who assumed a simple diagonal transition path and carried out constrained minimization as a neighboring carbon atom is moved to the vacancy site. The migration energy results, given in Table VI, show significant discrepancy between the present model for ZrC and the calculation for TiC using the tight-binding potential.[12] Using radioactive tracer technique, Sarian *et al.*[48,49] have reported the bulk diffusion constant of carbon atoms in ZrC to be 1.62×10^2 exp(-113200/RT) cm^2/s, which converts to an activation energy of $Q=4.904$ eV for carbon vacancy diffusion. Harris and Bristowe have argued that this is in good agreement with the tight-binding results, since $1.50+2.66=4.16$ eV.[47] We believe that another interpretation is more likely. Sarian has noted[49,50] that the activation energy for carbon vacancy diffusion should be the migration energy only, since there exists already ample amount of carbon vacancies in the lattice, even at 0 K. In the earlier experiment, the sample used was $ZrC_{0.965}$.[48] It seems unlikely that at this very large pre-existent vacancy density, thermal activation can still increase the vacancy density as a function of T as much as the Boltzmann factor exp($-E_f/k_BT$) suggests. If the thermal activation energy should consist of only the migration energy, then our migration energy result of 4.86 eV is in good agreement with the experiment.

C. Metal vacancy formation and migration energies

Using the GGA density functional and ultrasoft pseudopotential,[36] we compute the Zr vacancy formation energy, defined here as the energy cost of removing one Zr atom from B1–ZrC bulk and place it in hcp Zr. We use a 63-atom supercell and $7\times7\times7$ Monkhorst–Pack[45] **k** sampling. The planewave basis has an energy cutoff of 358.4 eV.

TABLE VII. Metal vacancy formation and migration energies in B1–ZrC/TiC.

	Formation (eV)	Migration (eV)	Total (eV)
TB (TiC)[a]	2.37	4.16	6.53
VASP (ZrC)	8.89	···	···
Present (ZrC)	5.80	···	···

[a]See Ref. 47.

Ion relaxation terminates when the energy change between two steps is less than 1 meV, and the maximum force on one atom is less than 0.015 eV/Å. We find that $E_f(\mathrm{V_{Zr}})=8.89$ eV from VASP. In contrast, the present model gives $E_f(\mathrm{V_{Zr}})=5.80$ eV. The results are tabulated in Table VII. We note that the Schottky pair formation energy (independent of pure element reference states), is $1.16+8.89-1.72=8.33$ eV from VASP, but is only $1.51+5.80-2.47=4.84$ eV from the present model.

In contrast to the case of the carbon vacancy, the agreement in forces near an unrelaxed Zr vacancy turns out to be not so bad. For the nearest six C atoms, the outward expansion force is 1.04 eV/Å from VASP, and 0.74 eV/Å from the present model. For the 12 second nearest Zr atoms, the inward contraction force is (0.40,0.40,0) eV/Å from VASP, and (0.43,0.43,0) eV/Å from the present model. Forces on other atoms are negligibly small. Energy decrease during the relaxation: $E_f^{\mathrm{unrelax}}(\mathrm{V_{Zr}})-E_f(\mathrm{V_{Zr}})$, is 0.38 eV in VASP and 0.23 eV in the present model.

Sarian[50] measured the diffusion constant of ^{44}Ti in TiC to be 4.36×10^4 exp$(-176\,400\pm3600/\mathrm{RT})$ cm^2/s, which converts to an activation energy of $Q=7.642\pm0.156$ eV. Unlike carbon vacancy, since there are no pre-existent metal vacancies in the system, the activation energy of metal atom diffusion should be the sum of formation and migration energies. However, as the metal atom (vacancy) has a larger size, it is conceivable that it has a more complex migration path, perhaps through C vacancy in a two-atom ring mechanism.

D. Bond shrinkage near vacancies

Aside from the formation and migration energies, it is helpful to look at the local geometry near a carbon vacancy,[12] as Moisy–Maurice *et al.* have measured the relevant quantities in $\mathrm{TiC_{0.76}}$ using elastic diffuse neutron scattering.[51] Figure 11 illustrates the atomic arrangements near a carbon vacancy. We will focus on the shrinkage of the nearest C–M bond pointing to the vacancy with relaxation direction indicated by the arrow. The results are shown in Table VIII.

There appears to be significant discrepancy between the experimental result and VASP result. At this point we would not conjecture which is more accurate. We note that the present model gives a shrinkage value that is quite close to the experimental result but is only 35% of the VASP result, which seems to correlate with the calculated outward expansion force ratio of $0.61/1.65=37\%$ near the unrelaxed carbon vacancy. We have also performed similar calculation for Zr vacancy, and find the C–M bond pointing to the Zr vacancy shrinks by 3.9% and 2.4% in VASP and the present model, respectively.

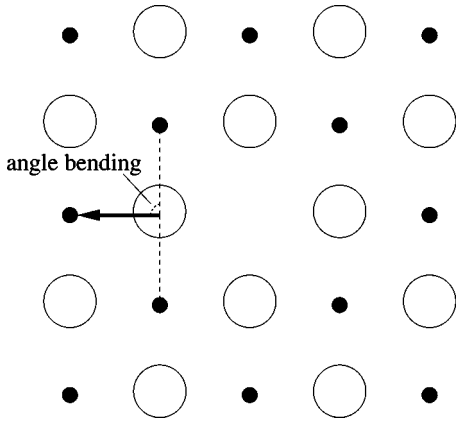

FIG. 11. Illustration of the shrinkage of the nearest C–M bond pointing to a carbon vacancy.

E. (001) surface relaxation

There had been controversy concerning the direction of the rumpled relaxation of TiC(001) surface.[11,52] Recently it has become clear that the carbon atoms relax outward while the metal atoms relax inward.[53,54] Both the tight-binding model[11] and our potential give the opposite relaxation directions, with our magnitude being smaller. The results are tabulated in Table IX. As the present potential has only ten parameters in which 6 can be varied, it is difficult to capture such a subtle effect which has to do with the electric fields near the surface.[52]

We have also computed the ZrC(001) surface energy to be 0.1012 eV/Å^2, for which no results are available from the literature for comparison. Maerky *et al.*[55] measured the room temperature fracture toughness of single crystal $\mathrm{TiC_{0.96}}$ along (001) plane to be 1.5 MPa m$^{1/2}$, which converts to a critical strain energy release rate of 4.5 J/m^2. Assuming the Griffith law[56] $G_{IC}=2\gamma$ one can convert to a surface energy of 0.1404 eV/Å^2 for TiC(001). This is about 1/3 of the SiC(001) surface energy, therefore ZrC/TiC should be more brittle than SiC.

F. Grüneisen parameter and thermal expansion coefficient

We have numerically computed the mode-specific Grüneisen parameter[39] at 0 K:

$$\gamma_k \equiv -\left(\frac{d\log\omega_k}{d\log\Omega}\right), \tag{18}$$

TABLE VIII. Shrinkage of the nearest C–Zr/Ti bond pointing to a carbon vacancy.

Shrinkage	TB (TiC)[a]	Exp't (TiC)[b]	VASP (ZrC)	Present (ZrC)
(Å)	0.1	0.03	0.081	0.028
(%)	4.6	1.4	3.4	1.2

[a]See Ref. 12.
[b]See Ref. 51.

TABLE IX. Rumpled relaxation of ZrC/TiC(001) surface.

	FPLMTO (TiC)[a]	Exp't (TiC)[b]	TB (TiC)[c]	Present (ZrC)
$z_C - z_M$ (Å)	0.05	0.076	−0.07	−0.0314

[a]See Ref. 52.
[b]See Ref. 53.
[c]See Ref. 11.

where ω_k is the frequency of a specific phonon mode k and Ω is the atomic volume. γ_k is then averaged with the mode-specific heat capacity $c_v(k)$:[39]

$$c_v(k) \equiv \frac{\hbar^2 \omega_k^2}{k_B T^2} \cdot \frac{e^{\hbar\omega_k/k_B T}}{(e^{\hbar\omega_k/k_B T}-1)^2}, \tag{19}$$

to give the overall Grüneisen parameter $\gamma(T)$, plotted in Fig. 12. The high-temperature limit agrees well with a published value of 1.33 for TiC using the all-electron full-potential linearized augmented plane-wave method.[57]

The total $C_V(T)$ is obtained by summing Eq. (19). The thermal expansion coefficient can then be obtained from

$$\alpha(T) \equiv \frac{1}{3} \cdot \frac{\partial \log \Omega}{\partial T}\bigg|_{P=0} = \frac{C_V(T)\gamma(T)}{3B(T)}. \tag{20}$$

As shown in Fig. 13, it is in excellent agreement with the experimentally measured 6.7×10^{-6}/K at high T.

$C_P(T)$ can be calculated as[58]

$$C_P(T) = C_V(T) + 9\alpha(T)^2 B(T) T \Omega. \tag{21}$$

$C_V(T)$, $C_P(T)$, and the experimentally measured $C_P(T)$ for $ZrC_{0.96}$[1] are shown in Fig. 14. The agreement is satisfactory up to 1500 K, at which point the measured $C_P(T)$ starts to deviate significantly from the harmonic phonon predictions.[39] We think that reflects significant microstructural changes inside $ZrC_{0.96}$ related to the enhanced mobility of carbon vacancies.

If one uses the Debye function (Appendix) as an analytical approximation for $C_V(T)$, and match their values at 300 K, the only parameter in the model, the Debye temperature T_D, is determined to be 747 K, which is comparable with various experimental determinations (~649 K).[1] In our molecular dynamics (MD) simulations, we will use this Debye function and the integral of correspondent zero-point energies in a quantum to classical temperature rescaling procedure[59] to ensure the correct limiting behavior at low T.

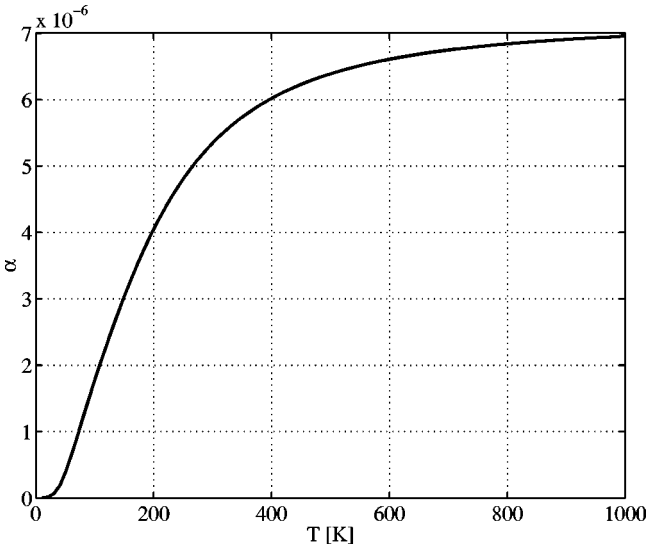

FIG. 13. Thermal expansion coefficient derived from the overall 0 K Grüneisen parameter.

G. Vibrational amplitudes and melting

The vibrational amplitudes of Zr and C atoms in B1–ZrC are calculated separately using phonon theory. They are shown in Fig. 15 along with x-ray diffraction measurements.[60] According to the Lindemann/Gilvarry rule,[61] a crystal melts when the atomic vibrational amplitudes reach a certain empirical fraction of the nearest neighbor distance. Figure 15 suggests a melting point around 3500 K.

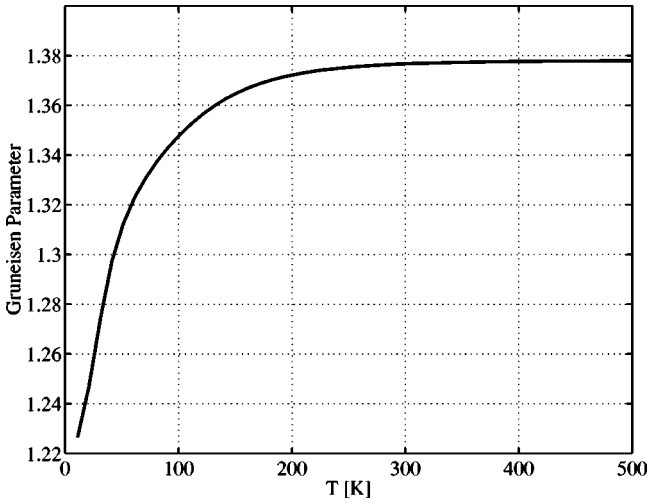

FIG. 12. Grüneisen parameter of ZrC as a function of T using $T=0$ phonon frequencies.

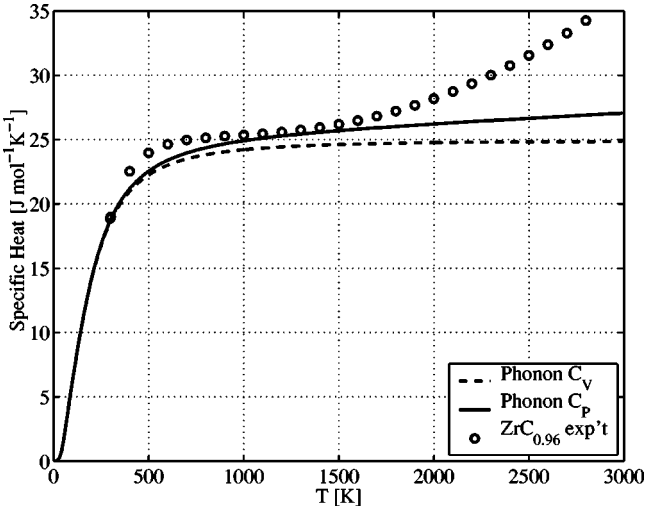

FIG. 14. Calculated heat capacities of ZrC using phonon frequencies at 0 K. The circles are experimentally measured C_P for $ZrC_{0.96}$ (see Ref. 1).

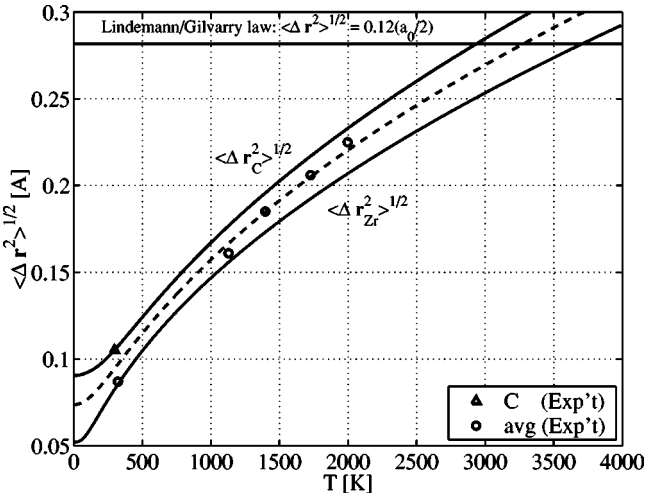

FIG. 15. Vibrational amplitudes of Zr and C atoms in B1–ZrC (dash line is the average $\sqrt{0.5(\langle|\Delta\mathbf{r}_{\mathrm{Zr}}|^2\rangle+\langle|\Delta\mathbf{r}_{\mathrm{C}}|^2\rangle}$, and Lindemann's law's prediction of the melting point. One X-ray measurement of carbon atom's vibrational amplitude at room temperature is shown in triangle, and five so-called average-amplitude experimental points at other temperatures are shown in circles (see Ref. 58).

This prediction has been checked independently. We create a 1000-atom ZrC cubic crystallite cluster that has six free surfaces, and slowly raise its temperature in a MD simulation. At elevated temperatures one expects to see some disordering on the surfaces, but we do not consider the crystallite to have started melting as long as it maintains its overall cubic shape. Of particular interest are the eight vertices of the cube; when they all start to collapse, it is a sign that surface tension has taken control and melting has begun.

In the simulation we find that the cubic configuration is stable up to 3400 K [Fig. 16(a)], but takes on a droplet shape when T is increased to 3650 K [Fig. 16(b)]. Therefore, the melting point should be around 3500 K, which may be compared with the experimental value of 3700 K.[1]

H. Thermal expansion simulation

A direct MD heating simulation is performed where T is slowly raised from 300 to 2500 K. The temperature rescaling scheme[59] using the Debye model is implemented (see Appendix). Figure 17 shows the agreement between our results and the experimentally measured thermal strains.[60]

VI. APPLICATIONS AND CONCLUDING REMARKS

Since our purpose of developing the potential model was to initiate the atomistic modeling of thermomechanical behavior of ZrC_X, we briefly discuss two such applications. Using the present model, we have determined the lattice thermal conductivity of ZrC_X through the Green–Kubo formalism in linear response theory, with heat current correlation obtained directly by molecular dynamics simulation.[62,63] The results show that the lattice vibrational component at realistic carbon vacancy concentrations is only a small part of the total conductivity, thus providing quantitative evidence that the primary mechanism for thermal conduction is electronic in nature. Previously we have been successful in predicting

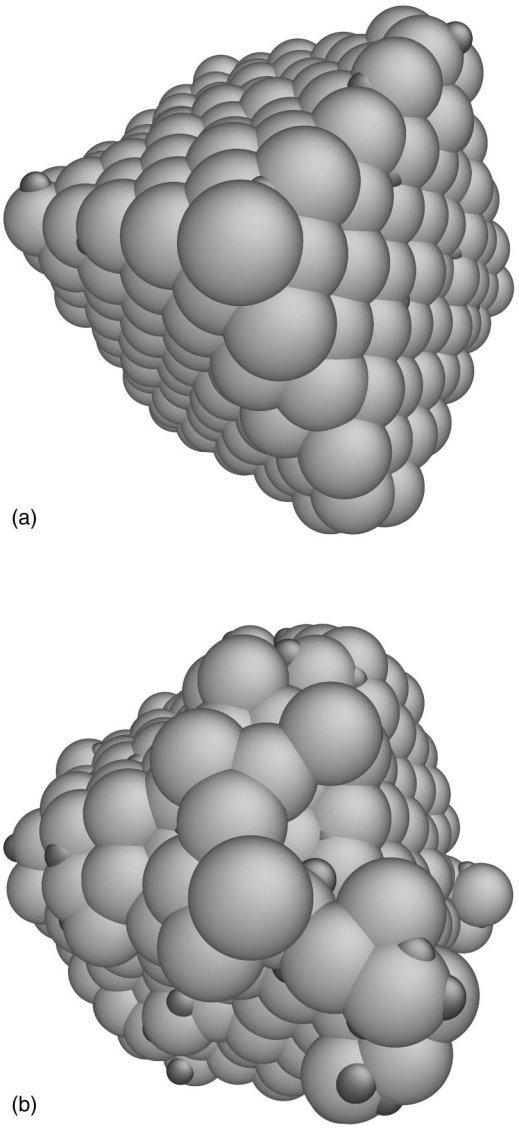

FIG. 16. (a) Cluster configuration at 3400 K. (b) Cluster configuration at 3650 K.

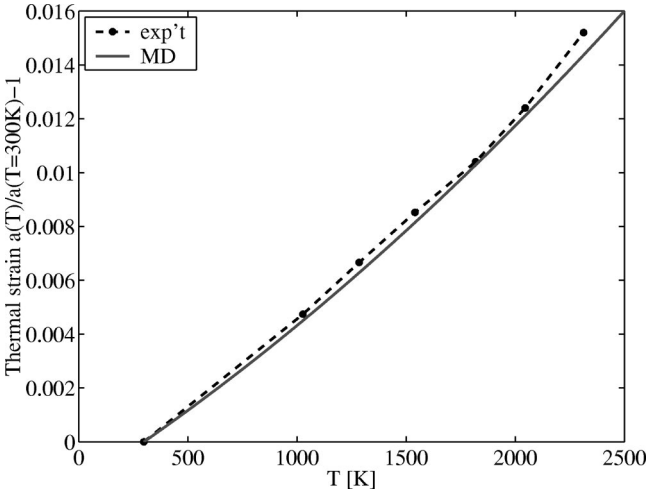

FIG. 17. Thermal strain measured in experiment (see Ref. 58) and from a direct MD simulation.

the thermal conductivity of SiC using a bond-order model which treats the interactions as purely covalent.[5] This gives us confidence that the simulation results can be predictive, which in turn allows us to address an important question concerning the relative magnitudes of the vibrational and electronic contributions to the thermal conductivity of ZrC_X.

Using the present potential model, we have also studied the deformational response of ZrC to an external stress in single crystal and nanocrystalline forms.[62,64,65] From molecular dynamics simulation of the extension of a nanocrack under uniaxial tension we obtained a fracture toughness value of 1.1 MPa $m^{1/2}$ using the Griffith criterion for brittle cracks, comparable to an experimental value of 1.5 MPa $m^{1/2}$ for Ti $C_{0.96}$.[55] In the study of yielding of a nanocrystalline sample to an applied shear, we observed increasing shear strength with increasing grain size in the range of 2.5–6 nm. This suggests that an inverse Hall–Petch behavior which has been previously reported in simulations of an elemental metal[66] could also operate in a ceramic material. In both cases, the dominant mechanism for the behavior appears to be controlled by small-scale sliding in the grain-boundary regions.

In this article we have described in detail the construction of a classical potential for ZrC_X based on considerations of the essential bonding characteristics of the system, the use of empirically modified, angular-dependent second-moment approximation functional form to characterize the interatomic interactions, and an emphasis on describing accurately the atomic force constants of B1–ZrC using the theoretical predictions of the DFT. By explicit demonstrations we show the model potential is capable of describing properly a wide range of physical properties. We thus suggest that the present description could well serve as an appropriate template for other metallic ceramics, such as TiC and HfC.

ACKNOWLEDGMENTS

J.L., D.L. and S.Y. would like to acknowledge the support of Air Force Office of Scientific Research under Grant No. F49620-00-10082, and the National Science Foundation under Grant No. DMR-9980015. The authors would also like to acknowledge helpful suggestions by the referee on the interpretation of our model and the determination of vacancy formation energies.

APPENDIX: DEBYE FUNCTION FOR TEMPERATURE RESCALING

Debye proposed the following single-parameter phonon DOS[58]

$$dP = d\left(\frac{\omega}{\omega_{\mathrm{D}}}\right)^3, \quad \omega < \omega_{\mathrm{D}}, \quad 0,\ \omega \geqslant \omega_{\mathrm{D}}, \tag{A1}$$

where P is the number of phonon states, ω is the phonon frequency and ω_{D} is the Debye frequency. Define $k_B T_D \equiv \hbar \omega_D$, we have the quantum energy average

$$\langle E \rangle = k_B T_D \left(\frac{T}{T_D}\right)^4 \int_0^{\frac{T_D}{T}} dy \left(\frac{1}{2} + \frac{1}{e^y - 1}\right) 3y^3. \tag{A2}$$

Therefore, if we require the classical system to have equal energy as the quantum system,[59] we would demand

$$T_{\mathrm{MD}} = T_D \left(\frac{T}{T_D}\right)^4 \int_0^{\frac{T_D}{T}} dy \left(\frac{1}{2} + \frac{1}{e^y - 1}\right) 3y^3. \tag{A3}$$

When $T \to 0$, $T_{\mathrm{MD}} \to (3/8) T_D$, a nonzero value. But when $T \to \infty$, $T_{\mathrm{MD}} = T + \mathcal{O}(1/T)$.

To obtain dT_{MD}/dT which is useful for thermal conductivity calculations,[5] we use

$$\frac{dT_{\mathrm{MD}}}{dT} = \left(\frac{T}{T_D}\right)^3 \int_0^{\frac{T_D}{T}} dy \frac{3y^4 e^y}{(e^y - 1)^2} \equiv D\left(\frac{T}{T_D}\right), \tag{A4}$$

where $D(x)$ is the Debye function.[58] $D(x) \sim (4\pi^4/5)x^3$ as $x \sim 0$, and $D(x) \to 1$ as $x \to \infty$. In reality, the phonon DOS is of course not in the form of Eq. (A1), but Eqs. (A3) and (A4) nonetheless provide good functional forms for numerical representations of $T_{\mathrm{MD}}(T)$ and dT_{MD}/dT.

[1] L. E. Toth, *Transition Metal Carbides and Nitrides* (Academic, New York, 1971).
[2] M. Tang and S. Yip, Phys. Rev. B **52**, 15150 (1995).
[3] M. Tang and S. Yip, Phys. Rev. Lett. **75**, 2738 (1995).
[4] L. J. Porter, J. Li, and S. Yip, J. Nucl. Mater. **246**, 53 (1997).
[5] J. Li, L. J. Porter, and S. Yip, J. Nucl. Mater. **255**, 139-152 (1998).
[6] J. Tersoff, Phys. Rev. B **49**, 16349 (1994).
[7] H. C. Huang, N. M. Ghoniem, J. K. Wong, and M. I. Baskes, Modell. Simul. Mater. Sci. Eng. **3**, 615 (1995).
[8] J. Tersoff, Phys. Rev. B **37**, 6991 (1988).
[9] F. Willaime and C. Massobrio, Phys. Rev. Lett. **63**, 2244 (1989).
[10] F. Willaime and C. Massobrio, Phys. Rev. B **43**, 11653 (1991).
[11] K. E. Tan, A. P. Horsfield, D. Nguyen-Manh, D. G. Pettifor, and A. P. Sutton, Phys. Rev. Lett. **76**, 90 (1996).
[12] K. E. Tan, A. M. Bratkovsky, R. M. Harris, A. P. Horsfield, D. Nguyen-Manh, D. G. Pettifor, and A. P. Sutton, Modell. Simul. Mater. Sci. Eng. **5**, 187 (1997); errata: *ibid.* **6**, 335 (1998).
[13] Z.-W. Lu, D. Singh, and H. Krakauer, Phys. Rev. B **36**, 7335 (1987).
[14] J. C. Slater, J. Chem. Phys. **41**, 3199 (1964); see also J. C. Slater, *Quantum Theory of Molecules and Solids* (McGraw-Hill, New York, 1963–1974), Vol. 2, Table 3-1.
[15] A. Aguayo, G. Murrieta, and R. de Coss, Phys. Rev. B **65**, 092106 (2002).
[16] P. T. Jochym and K. Parlinski, Eur. Phys. J. B **15**, 265 (2000).
[17] S.-H. Jhi and J. Ihm, Phys. Rev. B **56**, 13826 (1997).
[18] F. H. Stillinger and T. A. Weber, Phys. Rev. B **31**, 5262 (1985).
[19] D. W. Brenner, Phys. Rev. B **42**, 9458 (1990).
[20] M. I. Baskes, Phys. Rev. B **46**, 2727 (1992).
[21] M. I. Baskes and R. A. Johnson, Modell. Simul. Mater. Sci. Eng. **2**, 147 (1994).
[22] J. A. Moriarty, J. F. Belak, R. E. Rudd, P. Soderlind, F. H. Streitz, and L. H. Yang, J. Phys.: Condens. Matter **14**, 2825 (2002).
[23] D. G. Pettifor and I. I. Oleinik, Phys. Rev. Lett. **84**, 4124 (2000).
[24] M. S. Tang, C. Z. Wang, C. T. Chan, and K. M. Ho, Phys. Rev. B **53**, 979 (1996).
[25] M. W. Finnis and J. E. Sinclair, Philos. Mag. A **50**, 45 (1984); erratum, *ibid.* **53**, 161 (1986).
[26] A. P. Sutton, *Electronic Structure of Materials* (Oxford University Press, Oxford, 1993).
[27] M. G. Fernandes and V. Pontikis, Mater. Sci. Forum **207**, 173 (1996); see also, M. G. Fernandes, Ph.D. thesis, Massachusetts Institute of Technology, 1996.
[28] A. H. Cottrell, *Chemical Bonding in Transition Metal Carbides* (Institute of Materials, London, 1995).
[29] F. Cyrot-Lackmann, J. Phys. Chem. Solids **29**, 1235 (1968).
[30] W. A. Harrison, *Electronic Structure and the Properties of Solids: The Physics of the Chemical Bond* (W. H. Freeman, San Francisco, 1980).
[31] G. J. Ackland and V. Vitek, Phys. Rev. B **41**, 10324 (1990).
[32] G. J. Ackland, D. J. Bacon, A. F. Calder, and T. Harry, Philos. Mag. A **75**, 713 (1997).
[33] N. I. Papanicolaou, G. C. Kallinteris, G. A. Evangelakis, D. A. Papacon-

statopoulos, and M. J. Mehl, J. Phys.: Condens. Matter **10**, 10979 (1998).
[34] B. A. Pailthorpe, D. Mitchell, and N. S. Bordes, Thin Solid Films **332**, 109 (1998).
[35] F. Ercolessi and J. B. Adams, Europhys. Lett. **26**, 583 (1994).
[36] G. Kresse and J. Hafner, Phys. Rev. B **47**, 558 (1993); G. Kresse and J. Furthmüller, *ibid.* **l54**, 11169 (1996).
[37] J. P. Perdew and Y. Wang, Phys. Rev. B **46**, 6671 (1992).
[38] M. I. Baskes, Phys. Rev. Lett. **83**, 2592 (1999).
[39] M. Born and K. Huang, *Dynamical Theory of Crystal Lattices* (Clarendon, Oxford, 1956).
[40] H. G. Smith, N. Wakabayashi, and M. Mostoller, in *Phonon Anomalies in Transition Metals, Alloys and Compounds, Superconductivity in d- and f-Band Metals*, Second Rochester Conference, edited by D. H. Douglas (Plenum, New York, 1976), p. 223.
[41] A. F. Guillermet, J. Alloys Compd. **217**, 69 (1995).
[42] C. Kral, W. Lengauer, D. Rafaja, and P. Ettmayer, J. Alloys Compd. **265**, 215 (1998).
[43] W. S. Williams, JOM-Journal of the Minerals Metals & Materials Society **50**, 62 (1998).
[44] D. L. Price and B. R. Cooper, Phys. Rev. B **39**, 4945 (1989).
[45] H. J. Monkhorst and J. D. Pack, Phys. Rev. B **13**, 5188 (1976).
[46] M. I. Baskes, M. Asta, and S. G. Srinivasan, Philos. Mag. A **81**, 991 (2001).
[47] R. M. Harris and P. D. Bristowe, Philos. Mag. A **79**, 705 (1999).
[48] S. Sarian and J. M. Criscione, J. Appl. Phys. **38**, 1794 (1967).
[49] S. Sarian, J. Appl. Phys. **39**, 3305 (1968).
[50] S. Sarian, J. Appl. Phys. **40**, 3515 (1969).
[51] V. Moisy-Maurice, C. H. de Novion, A. N. Christensen, and W. Just, Solid State Commun. **39**, 661 (1981).
[52] D. L. Price, J. M. Wills, and B. R. Cooper, Phys. Rev. Lett. **77**, 3375 (1996).
[53] Y. Kido, T. Nishimura, Y. Hoshino, S. Otani, and R. Souda, Phys. Rev. B **61**, 1748 (2000).
[54] K. Kobayashi, Jpn. J. Appl. Phys., **39**, 4311 (2000).
[55] C. Maerky, M. O. Guillou, J. L. Henshall, and R. M. Hooper, Mater. Sci. Eng., A **209**, 329 (1996).
[56] T. L. Anderson, *Fracture Mechanics: Fundamentals and Applications*, 2nd ed. (CRC Press, Boca Raton, 1995).
[57] W. Wolf, R. Podloucky, T. Antretter, and F. D. Fisher, Philos. Mag. B **79**, 839 (1999).
[58] D. A. McQuarrie, *Statistical Mechanics* (Harper Collins, New York, 1976).
[59] Y. H. Lee, R. Biswas, C. M. Soukoulis, C. T. Chan, and K. M. Ho, Phys. Rev. B **43**, 6573 (1991).
[60] C. R. Houska, J. Phys. Chem. Solids **25**, 359 (1964).
[61] J. J. Gilvarry, Phys. Rev. **102**, 308 (1956).
[62] J. Li, Ph.D. thesis, MIT, August 2000.
[63] J. Li, D. Liao, and S. Yip (unpublished).
[64] D. Liao, Ph.D. thesis, MIT, August 2001.
[65] D. Liao, J. Li, and S. Yip (unpublished).
[66] J. Schiotz, F. D. Di Tolla, and K. W. Jacobsen, Nature (London) **391**, 561 (1998).